nature geoscience

Article

https://doi.org/10.1038/s41561-025-01707-2

Near-field evidence for early supershear rupture of the M_w 7.8 Kahramanmaraş earthquake in Turkey

Received: 12 March 2023

Accepted: 23 April 2025

Ares Rosakis [1], **Mohamed Abdelmeguid** [1,4] & **Ahmed Elbanna** [2,3,4]

The M_w 7.8 Kahramanmaraş/Pazarcik earthquake was larger and more destructive than was expected based on historical seismicity in southeastern Turkey in the past few centuries, raising questions about the nature of rupture initiation and propagation. Here we analyse near-field ground velocity records from seismometers to constrain the rupture propagation speed along the Narli splay fault, which hosted the initial rupture that eventually reached the main East Anatolian Fault. The measured particle velocities provide evidence for an early transition of the rupture from sub-Rayleigh to supershear behaviour, whereby the rupture speed exceeds that of the seismic shear waves. The near-in-situ field observational evidence is consistent with mechanistic understanding of supershear rupture. We estimate the instantaneous supershear rupture propagation speed to have been 1.55 times that of the shear wave speed and the sub-Rayleigh-to-supershear transition length to have been around 19.45 km. This work reveals the value of near-field instrumentation in characterizing the initiation of earthquakes along major faults.

On 6 February 2023, a moment magnitude (M_w) 7.8 earthquake shook the southeastern parts of Turkey and northern Syria. Preliminary back projection models based on teleseismic data and multiple seismic inversions suggest that rupture initiated at 1:17:35.5 coordinated universal time on the Narli splay fault in near proximity to the East Anatolian Fault (EAF)[1]. The preliminary hypocentre location (retrieved on 12 February 2023) was estimated by the Turkish Disaster and Emergency Management Authority (AFAD) to be 37.288° N, 37.042° E[2] with a depth of approximately 8 km, whereas the US Geological Survey (USGS) estimated it to be 37.166° N, 37.042° E ± 6.3 km (as indicated by the red star marker in Fig. 1) with a depth of approximately 18 ± 3 km (ref. 1). Current estimates of the depth (retrieved on 20 February 2023) have been updated to be 10 ± 2 km (ref. 1). The rupture then propagated northeast, subsequently transferring to the EAF and starting a sequence of seismic events[3,4]. Furthermore, subsequent geodetic and seismic inversions confirmed the multi-segment nature of the M_w 7.8 rupture[3,5–7]. The sequence of events resulted in catastrophic levels of destruction with substantial humanitarian and financial losses. Based on historical records in the past several hundred years, the magnitude of the event and total rupture length were both much larger than expected for southern Turkey[8–15]. This, together with the intensity of the measured ground shaking[16], motivated us to investigate the nature of rupture initiation, early propagation and the possibility of early supershear transition.

Although consensus has been reached regarding the complexity of the M_w 7.8 earthquake and its scale[6,17–19], the rupture propagation speed remains highly debated, particularly with regard to the presence of supershear ruptures[3,5,7,20,21]. Kinematic inversions provide great insight into the history of slip accumulation, but they could overlook important rupture physics under specific circumstances due to: grid resolution; trade-offs between different constraints

---

[1]Graduate Aerospace Laboratories, California Institute of Technology, Pasadena, CA, USA. [2]Department of Civil and Environmental Engineering, University of Illinois at Urbana–Champaign, Urbana, IL, USA. [3]Beckman Institute for Advanced Science and Technology, University of Illinois at Urbana–Champaign, Urbana, IL, USA. [4]These authors contributed equally: Mohamed Abdelmeguid, Ahmed Elbanna. e-mail: arosakis@caltech.edu; meguid@caltech.edu; elbanna2@illinois.edu

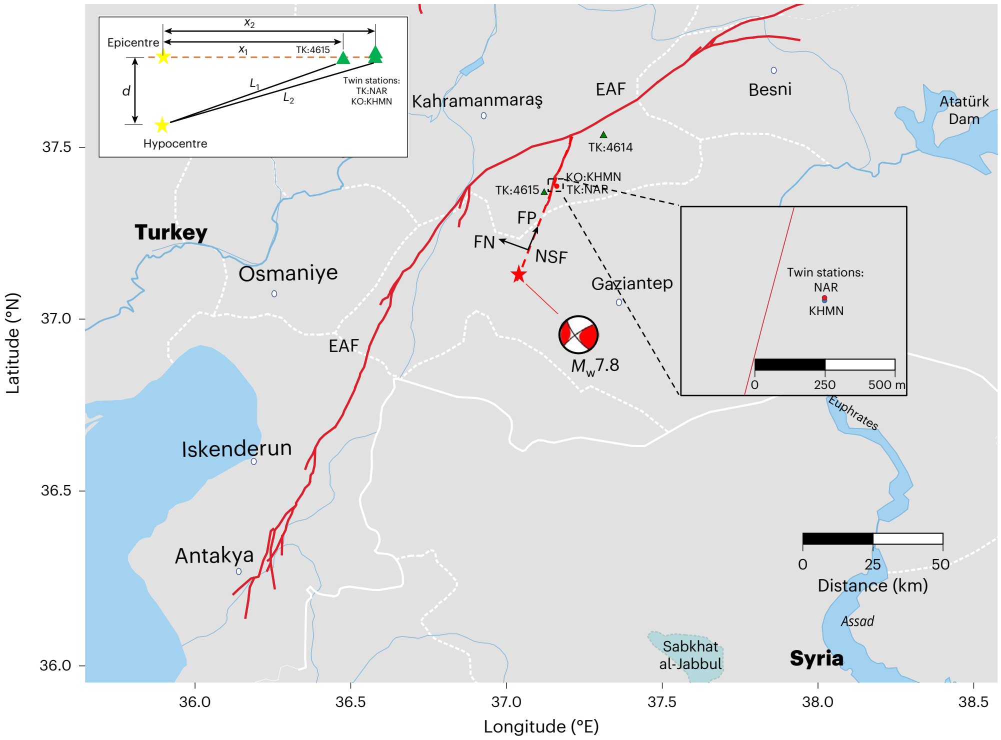

Fig. 1 | Map of the EAF zone, highlighting the estimated location and focal mechanism of the hypocentre of the M_w 7.8 Kahramanmaraş earthquake. The dashed red line represents the inferred splay fault (that is, the Narli splay fault (NSF)) trace based on the recorded seismicity obtained from AFAD. The red star indicates the USGS estimated hypocentre. The green triangles indicate the locations of the nearest seismic stations to the fault trace. The black arrows indicate the left lateral sense of motion of the fault. Inset: schematic of the relative epicentral and hypocentral locations (yellow stars) of the stations. Basemap from Natural Earth.

to improving global fits and minimizing overall error; decisions to include or exclude specific stations; and computational demand. For instance, local variations in rupture speeds over distances comparable to the grid size may be missed or averaged out and misfits in arrival times at specific stations may occur. This may explain why different inversion studies for this event have reached different conclusions about the rupture speed in different parts of the fault. In this study, we focus on the initial rupture propagation phase that spanned the Narli fault. We couple extremely near-field data from strong ground motion seismometers with theoretical, experimental and historical understanding of sub-Rayleigh and supershear ruptures to constrain the rupture propagation speed along the Narli splay fault. This investigation was only possible due to the availability of near-field records from extremely close to the Narli fault that allowed us to constrain the rupture propagation speed along the fault based on a mechanistic understanding of rupture dynamics.

Figure 1 illustrates the estimated location of the hypocentre; the approximate strike of the Narli fault, which was inferred to be around 22° east of north based on the aftershock sequence; and the sense of motion, which was left lateral for both the Narli fault and the EAF[22]. To the best of our knowledge, four stations exist very close to the Narli fault, as highlighted by the green diamonds in Fig. 1. Two of these stations—TK:NAR and KO:KHMN—are located at 37.3919° N, 37.1574° E and 37.3916° N, 37.1574° E, respectively[2,23], and are referred to here as the twin stations because they are in very close proximity to one another (only 30 m apart). Station TK:4615 is located closer to the epicentre at 37.386° N, 37.138° E[2]. Station TK:4614 is the furthest from both the Narli fault and the epicentre and is located at 37.48513° N, 37.29775° E. The insert in Fig. 1 is a schematic of the positions of the stations, showing the distances x_1, x_2 relative to the epicentre and the distances L_1, L_2 relative to the hypocentre, located at depth d. These four stations provide a rare and detailed insight into the near-field characteristics of the rupture on the splay fault and indeed close examination of these records has revealed unique observations, which we describe below.

Evidence of supershear propagation

Figure 2a shows the time histories of the particle velocities along the fault parallel (FP), fault normal (FN) and fault vertical (FV) directions from the twin stations (TK:NAR and KO:KHMN). It is important to reiterate that these records correspond to two different instruments and, as a result, the good agreement between these two records obtained from two different seismic networks provides assurance regarding the quality of the data used in this study. Furthermore, the measurement agreement between the two independent records excludes, with a high degree of certainty, installation errors for any specific seismogram. The details for obtaining and processing the ground motion data are described in the Methods section 'Ground motion data'. The blue vertical dashed line in Fig. 2a indicates the estimated arrival of the primary wave (P wave) from the hypocentre, based on rupture initiation at the USGS-provided time of 1:17:35.5 coordinated universal time[1].

The velocity waveforms for the twin stations reveal unique characteristics. First, we observe that the FP component is larger than the FN component. This characteristic is atypical of sub-Rayleigh strike-slip earthquake ruptures, which feature more dominant FN versus FP velocity components. However, a dominant FP component is a characteristic feature of supershear ruptures[24,25] in which the rupture speed exceeds the shear wave (S-wave) speed of crustal rocks. Such behaviour has been observed in both the laboratory[26–28] and the field[25,27,29–31] and has also been predicted by theory[26,29,32–35]. The Methods section 'A geometric interpretation of the ground velocity field structure' and Extended Data Fig. 1 detail the geometrical basis for this mechanistic signature.

From the velocity waveforms, we measure the change in the velocity amplitude associated with the arrival of the supershear Mach cone at the station and we indicate this arrival using a red dashed line in

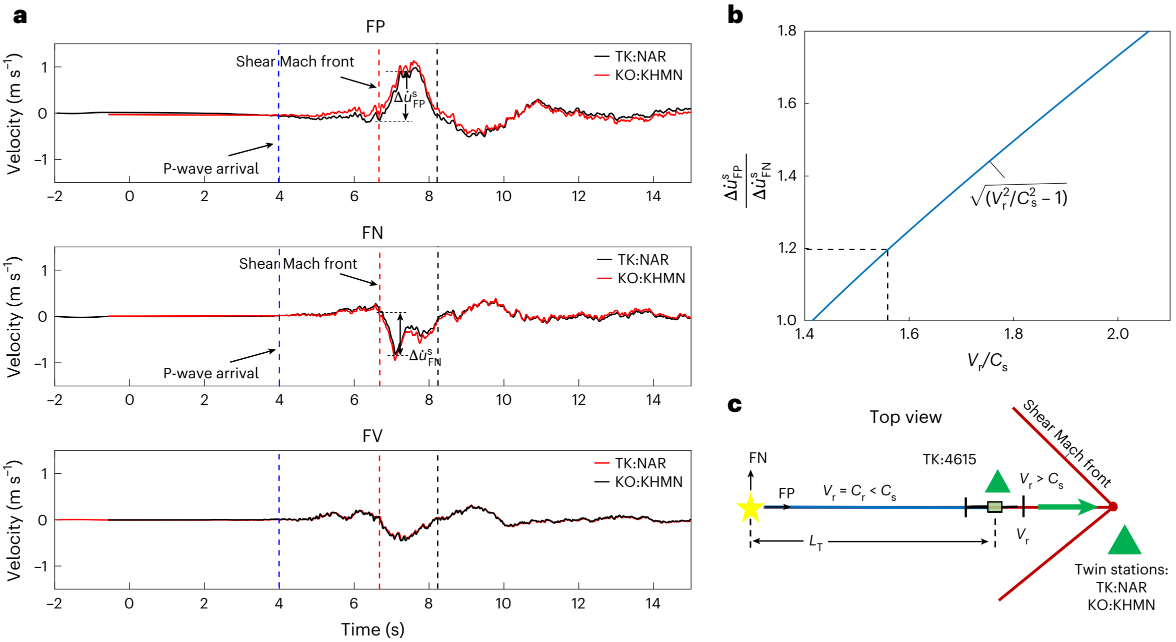

Fig. 2 | Supershear characteristics of near-field records at stations TK:NAR and KO:KHMN. **a**, Unfiltered instrument-corrected strong ground motion records of the FP, FN and FV particle velocities obtained at stations TK:NAR (solid black line) and KO:KHMN (solid red line). Note that the FP component is larger than the FN component, suggesting supershear rupture propagation. The blue dashed lines indicate the arrival of the P wave, the red dashed lines indicate the arrival of the shear Mach front and the black dashed lines indicate the extent of the velocity pulse. **b**, The ratio of FP to FN particle velocity is known to be a function of the rupture speed normalized by the S-wave speed. For a ratio of FP to FN velocity of ~1.2, the rupture propagates at approximately 1.55C_s as indicated by the black dashed lines. **c**, Schematic showing the top view on the surface, highlighting the locations of the stations (green triangles), as well as the arrival of the shear Mach front. The epicentre is marked by a yellow star. The transition point is marked by a green square and associated error bars. The green arrow indicates the rupture propagation direction. $V_r = C_r < C_s$ is indicated by a blue line and $V_r > C_s$ is indicated by a red line.

Fig. 2a. We observe that the ratio of the FP component ($\Delta\dot{u}^{s}_{FP}$) to the FN component ($\Delta\dot{u}^{s}_{FN}$) is approximately ~1.2. These changes in amplitude correspond to the shear part of the velocity signal and are due to the arrival of the shear Mach lines[26]. The ratio of the changes in the particle velocities in the two orthogonal directions has been theoretically shown by Mello et al.[26] to depend uniquely on the ratio of the rupture speed (V_r) and S-wave speed (C_s) as follows: $\Delta\dot{u}^{s}_{FP}/\Delta\dot{u}^{s}_{FN} = \sqrt{(V_r/C_s)^2 - 1}$. This relationship is also shown schematically in Fig. 2b. Accordingly, and as indicated in the figure, for a ratio of 1.2, the corresponding supershear rupture speed is ~1.55C_s. The ratio of the FP component to the FN component depends on the orientation of the Narli fault. To address the possible orientational uncertainty, we investigated the role of the fault strike on this ratio (Methods section 'Strike orientation uncertainty' and Extended Data Fig. 2) and found that the ratio $\Delta\dot{u}^{s}_{FP}/\Delta\dot{u}^{s}_{FN}$ was >1 for strike angles between 16 and 32°. A schematic of this supershear transition is shown in Fig. 2c, where we show a top view detailing the location of the three stations relative to the epicentre. We define a transition length L_T relative to the hypocentral distance after which the rupture speed V_r exceeds the S-wave speed C_s. Figure 2c also shows the interaction of the shear Mach cone with the stations. We consider the higher FP-to-FN component ratio the first key evidence for early supershear rupture, which we will further corroborate in subsequent sections.

We note that this evidence is independent of the hypocentre location and is not constrained by arrival times. It is based on the occurrence of a purely mechanistic signature characterizing supershear propagation. This signature can only be identified in very-near-fault records obtained from instruments located at distances less than a few kilometres away from the propagating rupture tip. This reliance on the nature of the local field of the dynamically propagating rupture eliminates errors due to uncertainty about the hypocentral location or event timing. Furthermore, although local site effects and heterogeneity could indeed contribute to the amplification of ground velocity records and affect individual component amplitudes, they have little influence on the ratio of FP to FN components, at least in the near-field region[36]. It has also been shown that surface effects could contribute to the transition to supershear propagation[37]. Finally, although an argument can be made that the uncharacteristically large increase in the FP component of velocity is due to directivity effects: (1) fault directivity effects are manifestations of the velocity field, which is inherently different for sub-Rayleigh and supershear earthquakes; and (2) several studies of rupture propagation along strike-slip faults have revealed that the directivity for strike-slip faulting further enhances the FN polarization[34,38–40], which would contradict the station record. Recent observations of oblique strike-slip faults suggest that supershear propagation near a free surface due to the heterogeneous slip-weakening distance can amplify the FP component, even while the rupture remains subshear within the bedrock[41]. However, for vertically dipping strike-slip faults such as the Narli fault, current dynamic rupture models show that FP amplification requires supershear propagation[34,42–44]. The existence of widespread precedent from historic earthquakes[29,45,46], highly instrumented laboratory experiments[26,27,32,47] and an extensive body of theoretical work[26,34,35,44,48,49] provides credence to our hypothesis that supershear rupture propagated through the twin stations, based on their recorded velocity waveforms.

We further support our hypothesis by exploring the arrival times at the nearby station TK:4614, which is located further away along the Narli fault. TK:4614 is located 16 km radially from the twin stations and ~9 km normal to the Narli fault. Although the location of TK:4614 precludes a similar analysis of the rupture-tip-induced velocity disturbance, we can still explore the arrival times at this station. The relative time it took for the shear disturbance to arrive at TK:4614 from the twin stations was ~4.1 s, which yields an average wave propagation speed of 3.9 km s^{-1} higher than the S-wave speed (Extended Data Fig. 3). In the Methods section 'Shock wave arrival

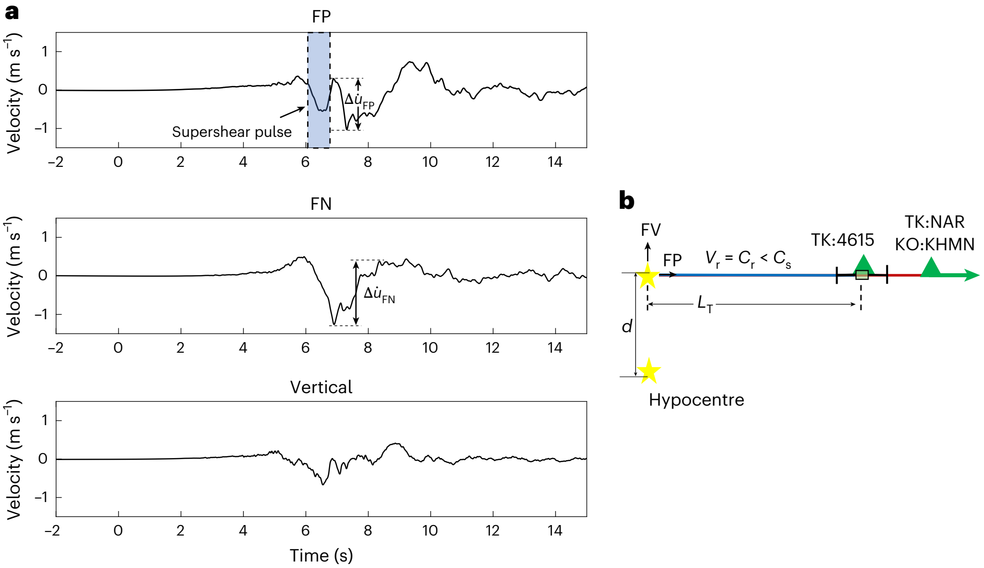

Fig. 3 | The transition from sub-Rayleigh to supershear rupture propagation was captured by the TK:4615 station. a, Strong ground motion records of the FP, FN and FV particle velocities. The highlighted region indicates the emergence of a supershear pulse ahead of the characteristic signature of a sub-Rayleigh rupture. **b**, Schematic of the locations of the stations (green triangles) relative to the epicentre and hypocentre (yellow stars). The transition point is marked by a green square with associated error bars. The green arrow indicates the rupture propagation direction. Station TK:4615 is located within close proximity to the transition point. $V_r = C_r < C_s$ is indicated by a blue line.

at station TK:4614', we further explore the possibility of shock wave arrival at station TK:4614. Utilizing the strong ground motion records shown in Extended Data Fig. 3b,c, we demonstrate several features that assert our hypothesis of supershear propagation on a portion of the Narli fault and rule out the possibility of sub-Rayleigh propagation between the two stations.

Signature of sub-Rayleigh-to-supershear transition

Next, we explore the ground motion characteristics of the closest station to the epicentre, TK:4615. Similar to Fig. 2a, Fig. 3a shows the time histories of the particle velocities along the FP, FN and FV directions, this time for TK:4615 (AFAD)[2]. However, this record is qualitatively different from the record shown in Fig. 2a. Indeed, we observe here that the FN velocity component is larger than the FP component, which is characteristic of a primarily sub-Rayleigh rupture. However, careful examination of the FP record indicates the presence of a small but well-defined pulse ahead of the Rayleigh signature, as indicated in the shaded region in the top panel of Fig. 3a. We believe that this feature is a supershear pulse formed ahead of the primary rupture, which was still propagating at the Rayleigh wave speed. Accordingly, we hypothesize that station TK:4615 is located very close to the point where the rupture transitioned from sub-Rayleigh to supershear.

To investigate the validity of our suspicions about supershear transition and the location of TK:4615, we present a preliminary analysis comparing the location of the station x_1 with our independent estimate of L_T obtained from the twin stations record shown in Fig. 2a. Based on the geometry of Fig. 2c, and assuming that the rupture tip initially propagates at $V_r = C_r$ before transition between (0, 0) and (0, L_T) and then transition to $V_r = 1.55C_s$ until it arrives at the twin stations at x_2, we can estimate a transition length L_T by further assuming that the stations are located on the fault[27,47].

$$L_T = C_R \frac{x_2 - t_s V_r}{C_R - V_r} \qquad (1)$$

where t_s is the arrival time of the shear Mach cone to the station, which can be obtained from Fig. 2a (red dashed line), and V_r is the supershear rupture speed $1.55C_s$. In the above relationship, x_2 is furnished as $\sqrt{L_2^2 - d^2}$, as shown in the insert of Fig. 1, where L_2 is the distance of the twin stations from the hypocentre at depth d. L_2 is estimated based on the P-wave arrival time (first disturbance) from the hypocentre location to the station, as well as the assumed dilatational wave speed, C_p.

We further assume $C_s = 3{,}320$ m s^{-1} and $C_p = 5{,}780$ m s^{-1}, which correspond to a Poisson's ratio of 0.25 and are in good agreement with velocity models for the southern Turkey region (refs. 50,51 and the references within). It follows then that $C_R = 3{,}050$ m s^{-1} and $V_r = 5{,}146$ m s^{-1}. Based on the arrival time of the P wave at the twin stations and using the above C_p leads to $L_2 = 23.7$ km. For a hypocentre depth of $d = 10.9$ km, equation (1) yields a transition length $L_T = 19.45$ km (Fig. 3b). We then use the P-wave arrival time at station TK:4615 to identify its distance from the hypocentre: $L_1 = 22.3$ km. Using the Pythagorean theorem, we compute the epicentral distance of station TK:4615 as $x_1 = 19.45$ km. For this particular choice of depth d, we observe that the location of the station TK:4615 coincides with the location of the sub-Rayleigh-to-supershear transition, which is consistent with our hypothesis. This estimated depth of 10.9 km is within the range predicted by the two agencies (AFAD and the USGS)[1,2]. We note that before 19 February 2023 the USGS estimated the depth to be 18 km, but later this was updated to be 10 ± 1.8 km (retrieved at 16:10 Pacific Standard Time on 20 February 2023), which is more in line with our independently obtained estimates. Furthermore, computing the distance between the twin stations and TK:4615 yields $\Delta x = x_2 - x_1 = 1.6$ km along the fault strike direction. Since the total distance between the twin stations and TK:4615 is ~2 km, based on their respective coordinates, this computed difference in their epicentral distances is a plausible estimate. The fact that we could independently constrain the depth of the hypocentre based on our purely mechanistic methodology of rupture propagation at supershear speeds represents another key finding of our study.

It should be noted that the probability of capturing the birth of supershear ruptures is very low. However, this transition has been reported experimentally in laboratory earthquakes[26,52] (we refer the reader to Fig. 14 in ref. 26 for illustration). Specifically, Mello et al.[26] captured this transition by comparing dynamic, full-field photoelastic images of the initial stages of the formation of the supershear pulse with near-fault particle velocity records measured at a location close to the transitioning rupture and by further correlating the two measurement techniques. The velocity records were obtained experimentally by a pair of laser velocimeters recording the FP and FN components[26]. Therefore, the velocity record at station TK:4615 provides a unique window into witnessing, in situ, the birth of a supershear earthquake.

Discussion

The 6 February 2023 Kahramanmaraş/Pazarcik earthquake sequence affecting Turkey and Syria initiated on the Narli splay fault in close proximity to the EAF. Our analysis of four rare near-field (~1 km from the Narli fault) ground velocity records suggests that the rupture that propagated on the Narli fault had transitioned from sub-Rayleigh to supershear speeds (V_r = ~$1.55C_s$) at an epicentral distance of approximately 19.45 km, and before reaching the EAF. The records obtained from the twin stations showing a higher FP component relative to the FN component are in agreement with characteristics observed in previous historical records[29,45,46,53,54], experimental observations[26,27] and theoretical interpretations of mode II dynamic fracture[26,55]. Furthermore, through numerical modelling of dynamic rupture propagation of the Turkey earthquake, it was also demonstrated that supershear propagation results in a larger FP velocity jump (the increase in particle velocity due to the passage of the rupture front) relative to that of FN[56]. The presence of two instruments (separated by 30 m) showing perfect agreement with one another provides confidence in the quality of the data used in the present study. In addition, the existence of a station located in such near proximity to the transition point is a unique occurrence. Knowledge of the transition point through station TK:4615 allowed us to constrain the depth of the earthquake to be ≤10.9 km.

The availability of these rare near-field records has allowed us to observe the mechanism of in situ transition from sub-Rayleigh to supershear rupture and provides a detailed window into the structure of near-fault particle motions in both FP and FN directions. The fact that multiple near-field stations captured the field dynamics of supershear rupture transition and propagation makes these records particularly important and emphasizes the value of having high-quality near-field data. Such data carry important local information about the rupture physics that is likely to be lost in far-field measurements[57]. This early supershear transition on the Narli fault may have enabled strong dynamic stress transfer to the nearby EAF and contributed to the continued rupture propagation to the northeast[58]. Indeed, previous studies have suggested that supershear ruptures are more effective in jumping across fault stepovers[59] and activating nearby faults[60–64]. However, the full dynamics of EAF activation requires an evaluation of the local stress fields, frictional characteristics and the geometry of the junction between the Narli fault and EAF. This is beyond the scope of the current study and is left for future investigation.

As alluded to in the introduction, the rupture propagation speed along both the Narli fault and EAF during the M_w 7.8 earthquake remains a highly contested topic. Large-scale inversions on the entire earthquake sequence using select strong ground motion and/or teleseismic data have provided conflicting conclusions. In one study, Melgar et al.[3] excluded the possibility of supershear rupture velocities throughout the event. However, in their analysis they excluded the stations we utilized here (that is, TK:NAR and TK:4615). Later studies by Okuwaki et al.[5] and Delouis et al.[7] suggested the possibility of supershear transients, with Delouis et al.[7] including the two stations in their global fit. Based on rupture phase analysis, Yao and Yang[65] suggested that on average the propagation speed on the southwestern segment of the EAF was between 3.1 and 3.4 km s^{-1}. However, they did not comment on the northeastern segment or the initial propagation on the Narli splay fault due to insufficient constraints. We note here that average propagation speeds between 3.1 and 3.4 km s^{-1} are considered relatively high given that in one-dimensional (1D) velocity models for this region the S-wave speed for the depth where most slip occurred (0–12 km) is 2.23 km s^{-1} for the top 2 km and up to 3.46 km s^{-1} for depths between 10 and 12 km (ref. 50).

In their detailed analysis of the Narli fault, Delouis et al.[7] suggest that the rupture propagation can be modelled using a constant subshear velocity. However, their results for the stations located near the Narli fault show that a 3.0 km s^{-1} average rupture speed on the splay fault provides the best fit, and this exceeds the S-wave speed in their homogeneous half-space model (C_s = 2.83 km s^{-1}). The authors argue that good agreement can be obtained at a rupture speed of 2.5 km s^{-1}, but we note that, based on their results, a relatively good fit can still be obtained at higher rupture speeds up to 3.3 km s^{-1}. It is important to note that their predicted rupture speed range on the Narli fault appears to be supershear with respect to the local velocity of the shallow layer in their 1D velocity model[50], which indirectly supports the interpretation of the dominance of the FP component over the FN component in the ground motion records analysed here. Sediment layers have been shown to contribute to the amplification of FP ground velocity. Recent numerical models revealed that although FN > FP does not rule out local supershear within the sediments, FP > FN remains a characteristic of global supershear propagation[42].

Whether an FP velocity jump that is higher than an FN velocity jump indicates supershear propagation under all conditions remains an open question for future research. For example, Kearse et al.[41] demonstrated that an oblique strike-slip fault (with a 70° dip angle) can potentially yield asymmetric wave particle velocities with a dominant FP component. These conditions may be interpreted as a result of supershear propagation in shallow sedimentary layers, even though the depth-averaged rupture speed could still be sub-Rayleigh. In the context of the current study, the Narli fault is a nearly vertical strike-slip fault. It follows that the conditions required to achieve the reported asymmetric ground motion are absent for the Narli fault. Furthermore, dynamic rupture models support the notion that FP > FN implies supershear conditions[34,42–44]. It is also important to highlight that although we use the FP > FN condition as initial evidence we also present additional supporting evidence that further corroborates our conclusion.

To further reconcile our observations of supershear transition on the Narli fault, as presented above, we also explore the phase arrival of strong ground motion at yet another station (TK:4611), which lies along the virtual extension of the Narli fault, past its junction with the EAF, and is located at a distance of 42 km from TK:NAR (the twin stations). This is discussed in the Methods section 'Station TK:4611'. Based on phase analysis of the S-wave arrival times shown in Extended Data Fig. 4a, we estimate that the wave field between TK:NAR and TK:4611 propagated at an average speed of ~4.2 km s^{-1}. Such a speed far exceeds the average S-wave speed of the region[50]. We attribute this fast wave arrival to the arrest phase of the supershear rupture, which propagated on the latter part of the splay fault before eventually transitioning to the EAF. Additionally, further data-constrained 3D dynamic rupture models confirm that the rupture does indeed transition along the splay fault[19,66,67].

Our assertion of the nature of the rupture speed on the Narli fault is supported by a few key evidences, including: (1) dominant FP-to-FN component jumps; (2) accurate hypocentre depth constraint based on our hypothesis; (3) shock wave arrival at station TK:4614 (Methods); and (4) phase arrival analysis at station TK:4611 (Methods). These provide a strong argument that the rupture that propagated on the Narli fault indeed transitioned to supershear at a distance approximately 20 km from the epicentre. Rapid supershear transition could occur due to on-fault stress or strength heterogeneities[68,69] or off-fault material complexities[70,71], which would influence the local fault strength parameter S (refs. 52,72,73) and favour a transition to supershear rupture over much shorter distances, L_T.

Based on dynamic rupture modelling of the junction, Abdelmeguid et al.[56] demonstrated that due to the supershear propagation on the Narli splay fault the rupture propagation towards the northeast direction along the EAF will also transition to supershear, whereas the southwest propagation will probably be sub-Rayleigh. The supershear propagation to the northeast direction was highlighted by multiple seismic source inversions[7,74–76]. Due to the non-uniform stress state, the supershear propagation could be episodic. These transient episodes are difficult to deduce using sparse far-field measurements. In conjunction with fault geometry complexity, these transient effects may lead to complex wave fields that mask the Mach cone characteristics in the far field. Additional material heterogeneity in the form of velocity changes may also contribute to the scattering of the Mach cone in the far field, making transient episodes more difficult to deduce[36,77]. This may explain the observations by Xu et al.[21] who conducted a waveform correlation analysis on the southwest segment and were not able to find any persistent Mach cone signatures in the far field. This study reveals faster rupture velocities along the segments that show a dominant FP component. However, due to the limitations of teleseismic data, back projections can only predict average rupture velocities.

Overall, we hope that further studies of the regional stress field and the structure of the ground motion records will reveal more details about the nature of this complex multi-segment rupture that led to such a large-scale human tragedy[17,18,22,78]. Future detailed numerical simulations and analogue experimental investigations are also needed to better constrain the dynamics of complex fault zones, such as the EAF zone, beyond what is available from historical records and regional scaling relations. This will help to reduce the impact of future hazards and better inform preparedness efforts. Finally, we highlight that fusing dynamic rupture mechanics concepts with detailed analysis of individual stations greatly enhances the information content that can be extracted from available data. Indeed, such an approach provides unique insights that are complementary to what can be obtained from global inversion models and is capable of uncovering details that are missed in these models. We hope that our contribution will incentivize researchers to adopt this mechanistically based perspective in seismic data analysis and encourage the deployment of near-fault instruments along known and active fault systems.

Online content

Any methods, additional references, Nature Portfolio reporting summaries, source data, extended data, supplementary information, acknowledgements, peer review information; details of author contributions and competing interests; and statements of data and code availability are available at https://doi.org/10.1038/s41561-025-01707-2.

References

1. *M 7.8 - Pazarcik Earthquake, Kahramanmaras Earthquake Sequence* (USGS, 2023); https://earthquake.usgs.gov/earthquakes/eventpage/us6000jllz/executive
2. AFAD. *Turkish National Strong Motion Network* (Department of Earthquake, Disaster and Emergency Management Authority, 1973); https://doi.org/10.7914/SN/TK
3. Melgar, D. et al. Sub- and super-shear ruptures during the 2023 M_w 7.8 and M_w 7.6 earthquake doublet in SE Türkiye. *Seismica* **2**, 1–10 (2023).
4. Barbot, S. et al. Slip distribution of the February 6, 2023 M_w 7.8 and M_w 7.6, Kahramanmaraş, Turkey earthquake sequence in the East Anatolian Fault zone. *Seismica* **2**, 1–17 (2023).
5. Okuwaki, R., Yagi, Y., Taymaz, T. & Hicks, S. P. Multi-scale rupture growth with alternating directions in a complex fault network during the 2023 south-eastern Turkiye and Syria earthquake doublet. *Geophys. Res. Lett.* **50**, e2023GL103480 (2023).
6. Zahradnik, J., Turhan, F., Sokos, E. & Gallovifç, F. Asperity-like (segmented) structure of the 6 February 2023 Turkish earthquakes. Preprint at *EarthArXiv* https://doi.org/10.31223/X5T666 (2023).
7. Delouis, B., van den Ende, M. & Ampuero, J.-P. Kinematic rupture model of the 6 February 2023 7.8 Türkiye earthquake from a large set of near-source strong-motion records combined with GNSS offsets reveals intermittent supershear rupture. *Bull. Seismol. Soc. Am.* **114**, 726–740 (2024).
8. Kartal, R. F., Kadirioğlu, F. T. & Zünbül, S. Kinematic of East Anatolian Fault and Dead Sea Fault. In *Proc. 17th Active Tectonic Research Group Workshop (ATAG 17)* (Akdeniz University, 2013); https://www.researchgate.net/publication/271852091
9. Ambraseys, N. N. Temporary seismic quiescence: SE Turkey. *Geophys. J. Int.* **96**, 311–331 (1989).
10. Ambraseys, N. N. & Jackson, J. A. Seismicity of the Sea of Marmara (Turkey) since 1500. *Geophys. J. Int.* **141**, F1–F6 (2000).
11. Emre, O. et al. Active fault database of Turkey. *Bull. Earthq. Eng* **16**, 3229–3275 (2018).
12. Melgar, D. et al. Rupture kinematics of 2020 January 24 M_w 6.7 Dofüanyol-Sivrice, Turkey earthquake on the East Anatolian Fault Zone imaged by space geodesy. *Geophys. J. Int.* **223**, 862–874 (2020).
13. Taymaz, T., Eyidogãn, H. & Jackson, J. Source parameters of large earthquakes in the East Anatolian Fault zone (Turkey). *Geophys. J. Int.* **106**, 537–550 (1991).
14. Taymaz, T. et al. Source mechanism and rupture process of the 24 January 2020 M_w 6.7 Doğanyol-Sivrice earthquake obtained from seismological waveform analysis and space geodetic observations on the East Anatolian Fault zone (Turkey). *Tectonophysics* **804**, 228745 (2021).
15. Xu, C. et al. Rapid source inversions of the 2023 SE Türkiye earthquakes with teleseismic and strong-motion data. *Earthq. Sci.* **36**, 316–327 (2023).
16. Wani, F. M., Vemuri, J. & Rajaram, C. Strong ground motion characteristics observed in the February 6, 2023 M_w 7. 7 Türkiye earthquake. *Earthq. Sci.* **37**, 241–262 (2024).
17. Mai, P. et al. The destructive earthquake doublet of 6 February 2023 in south-central Turkiye and northwestern Syria: initial observations and analyses. *Seism. Rec.* **3**, 105–115 (2023).
18. Goldberg, D. E. et al. Rapid characterization of the February 2023 Kahramanmaraş, Türkiye, earthquake sequence. *Seism. Rec.* **3**, 156–167 (2023).
19. Jia, Z. et al. The complex dynamics of the 2023 Kahramanmaraş, Turkey, M_w 7.8–7.7 earthquake doublet. *Science* **381**, 985–990 (2023).
20. Liu, C. et al. Complex multi-fault rupture and triggering during the 2023 earthquake doublet in southeastern Turkiye. *Nat. Commun.* **14**, 5564 (2023).
21. Xu, L. et al. The overall-subshear and multi-segment rupture of the 2023 M_w 7.8 Kahramanmaraş, Turkey earthquake in millennia supercycle. *Commun. Earth Environ.* **4**, 379 (2023).
22. Reitman, N. G. et al. Rapid surface rupture mapping from satellite data: the 2023 Kahramanmaraş, Turkey (Türkiye), earthquake sequence. *Seism. Rec.* **3**, 289–298 (2023).
23. Kandilli Observatory & Earthquake Research Institute, Boğaziçi University. *Kandilli Observatory and Earthquake Research Institute (KOERI)* (International Federation of Digital Seismograph Networks, 1971); https://doi.org/10.7914/SN/KO
24. Rosakis, A. J., Samudrala, O. & Coker, D. Cracks faster than the shear wave speed. *Science* **284**, 1337–1340 (1999).

25. Bouchon, M. et al. How fast is rupture during an earthquake? New insights from the 1999 Turkey earthquakes. *Geophys. Res. Lett.* **28**, 2723–2726 (2001).
26. Mello, M., Bhat, H. S. & Rosakis, A. J. Spatiotemporal properties of sub-Rayleigh and supershear rupture velocity fields: theory and experiments. *J. Mech. Phys. Solids* **93**, 153–181 (2016).
27. Mello, M., Bhat, H. S., Rosakis, A. J. & Kanamori, H. Reproducing the supershear portion of the 2002 Denali earthquake rupture in laboratory. *Earth Planet. Sci. Lett.* **387**, 89–96 (2014).
28. Lu, X., Rosakis, A. J. & Lapusta, N. Rupture modes in laboratory earthquakes: effect of fault prestress and nucleation conditions. *J. Geophys. Res.* **115**, 1–25 (2010).
29. Dunham, E. M. & Archuleta, R. J. Evidence for a supershear transient during the 2002 Denali Fault earthquake. *Bull. Seismol. Soc. Am.* **94**, 256–268 (2004).
30. Zeng, H., Wei, S. & Rosakis, A. A travel-time path calibration strategy for back-projection of large earthquakes and its application and validation through the segmented super-shear rupture imaging of the 2002 M_w 7.9 Denali earthquake. *J. Geophys. Res. Solid Earth* **127**, e2022JB024359 (2022).
31. Ellsworth, W. et al. Near-field ground motion of the 2002 Denali Fault, Alaska, earthquake recorded at pump station 10. *Earthq. Spectra* **20**, 597–615 (2004).
32. Mello, M., Bhat, H. S., Rosakis, A. J. & Kanamori, H. Identifying the unique ground motion signatures of supershear earthquakes: theory and experiments. *Tectonophysics* **493**, 297–326 (2010).
33. Dunham, E. M. & Bhat, H. S. Attenuation of radiated ground motion and stresses from three-dimensional supershear ruptures. *J. Geophys. Res.* **113**, 1–17 (2008).
34. Hu, F., Oglesby, D. D. & Chen, X. The near-fault ground motion characteristics of sustained and unsustained free surface-induced supershear rupture on strike-slip faults. *J. Geophys. Res. Solid Earth* **125**, e2019JB019039 (2020).
35. Xu, J., Chen, X., Liu, P. & Zhang, Z. Ground motion signatures of supershear ruptures in the Burridge-Andrews and free-surface-induced mechanisms. *Tectonophysics* **791**, 228570 (2020).
36. Vyas, J. C., Mai, P. M., Galis, M., Dunham, E. M. & Imperatori, W. Mach wave properties in the presence of source and medium heterogeneity. *Geophys. J. Int.* **214**, 2035–2052 (2018).
37. Kaneko, Y. & Lapusta, N. Supershear transition due to a free surface in 3-D simulations of spontaneous dynamic rupture on vertical strike-slip faults. *Tectonophysics* **493**, 272–284 (2010).
38. Somerville, P. G., Smith, N. F., Graves, R. W. & Abrahamson, N. A. Modification of empirical strong ground motion attenuation relations to include the amplitude and duration effects of rupture directivity. *Seismol. Res. Lett.* **68**, 199–222 (1997).
39. Bray, J. D. & Rodriguez-Marek, A. Characterization of forward-directivity ground motions in the near-fault region. *Soil Dyn. Earthq. Eng.* **24**, 815–828 (2004).
40. Wang, Y. & Day, S. M. Effects of off-fault inelasticity on near-fault directivity pulses. *J. Geophys. Res. Solid Earth* **125**, 1–29 (2020).
41. Kearse, J. et al. Strong asymmetry in near-fault ground velocity during an oblique strike-slip earthquake revealed by waveform particle motions and dynamic rupture simulations. *Seismica* **3**, 1–12 (2024).
42. Abdelmeguid, M., Elbanna, A. & Rosakis, A. Ground motion characteristics of subshear and supershear ruptures in the presence of sediment layers. *Geophys. J. Int.* **240**, 967–987 (2025).
43. Hu, F., Oglesby, D. D. & Chen, X. The effect of depth-dependent stress in controlling free-surface-induced supershear rupture on strike-slip faults. *J. Geophys. Res. Solid Earth* **126**, e2020JB021459 (2021).
44. Dunham, E. M. & Archuleta, R. J. Near-source ground motion from steady state dynamic rupture pulses. *Geophys. Res. Lett.* **32**, L03302 (2005).
45. Ellsworth, W. L. et al. Near-field ground motion of the 2002 Denali Fault, Alaska, earthquake recorded at pump station 10. *Earthq. Spectra* **20**, 597–615 (2004).
46. Amlani, F. et al. Supershear shock front contribution to the tsunami from the 2018 M_w 7.5 Palu, Indonesia earthquake. *Geophys. J. Int.* **230**, 2089–2097 (2022).
47. Rubino, V., Rosakis, A. J. & Lapusta, N. Spatiotemporal properties of sub-Rayleigh and supershear ruptures inferred from full-field dynamic imaging of laboratory experiments. *J. Geophys. Res. Solid Earth* **125**, 1–25 (2020).
48. Aagaard, B. T. & Heaton, T. H. Near-source ground motions from simulations of sustained intersonic and supersonic fault ruptures. *Bull. Seismol. Soc. Am.* **94**, 2064–2078 (2004).
49. Bernard, P. & Baumont, D. Shear Mach wave characterization for kinematic fault rupture models with constant supershear rupture velocity. *Geophys. J. Int.* **162**, 431–447 (2005).
50. Güvercin, S. E., Karabulut, H., Konca, A. O., Doßan, U. & Ergintav, S. Active seismotectonics of the East Anatolian Fault. *Geophys. J. Int.* **230**, 50–69 (2022).
51. Pousse-Beltran, L. et al. The 2020 M_w-6.8 Elazığ (Turkey) earthquake reveals rupture behavior of the East Anatolian Fault. *Geophys. Res. Lett.* **47**, e88136 (2020).
52. Xia, K., Rosakis, A. J. & Kanamori, H. Laboratory earthquakes: the sub-Rayleigh-to-supershear rupture transition. *Science* **303**, 1859–1861 (2004).
53. Archuleta, R. J. & Hartzell, S. H. Effects of fault finiteness on near-source ground motion. *Bull. Seismol. Soc. Am.* **71**, 939–957 (1981).
54. Hall, J. F., Heaton, T. H., Halling, M. W. & Wald, D. J. Near-source ground motion and its effects on flexible buildings. *Earthq. Spectra* **11**, 569–605 (1995).
55. Freund, L. B. The mechanics of dynamic shear crack propagation. *J. Geophys. Res.* **84**, 2199–2209 (1979).
56. Abdelmeguid, M. et al. Dynamics of episodic supershear in the 2023 M7.8 Kahramanmaraş/Pazarcik earthquake, revealed by near-field records and computational modeling. *Commun. Earth Environ.* **4**, 456 (2023).
57. Ben-Zion, Y. A critical data gap in earthquake physics. *Seismol. Res. Lett.* **90**, 1721–1722 (2019).
58. Das, S. The need to study speed. *Science* **317**, 905–906 (2007).
59. Harris, R. A. & Day, S. M. Dynamics of fault interaction: parallel strike-slip faults. *J. Geophys. Res.* **98**, 4461–4472 (1993).
60. Templeton, E. L. et al. Finite element simulations of dynamic shear rupture experiments and dynamic path selection along kinked and branched faults. *J. Geophys. Res.* **114**, B08304 (2009).
61. Rousseau, C.-E. & Rosakis, A. J. On the influence of fault bends on the growth of sub-Rayleigh and intersonic dynamic shear ruptures. *J. Geophys. Res.* **108**, 2411 (2003).
62. Rousseau, C. E. & Rosakis, A. J. Dynamic path selection along branched faults: experiments involving sub-Rayleigh and supershear ruptures. *J. Geophys. Res.* **114**, 1–15 (2009).
63. Bhat, H. S., Dmowska, R., Rice, J. R. & Kame, N. Dynamic slip transfer from the Denali to Totschunda Faults, Alaska: testing theory for fault branching. *Bull. Seismol. Soc. Am.* **94**, S202–S213 (2004).
64. Ma, X. & Elbanna, A. Dynamic rupture propagation on fault planes with explicit representation of short branches. *Earth Planet. Sci. Lett.* **523**, 115702 (2019).
65. Yao, S. & Yang, H. Rupture phases reveal geometry-related rupture propagation in a natural earthquake. *Sci. Adv.* **11**, 0154 (2025).

66. Wang, Z. et al. Dynamic rupture process of the M_w 7.8 Kahramanmaraş earthquake (SE Türkiye): variable rupture speed and implications for seismic hazard. *Geophys. Res. Lett.* **50**, e2023GL104787 (2023).
67. Gabriel, A.-A., Ulrich, T., Marchandon, M., Biemiller, J. & Rekoske, J. 3D dynamic rupture modeling of the 6 February 2023, Kahramanmaraş, Turkey M_w7.8 and 7.7 earthquake doublet using early observations. *Seism. Rec.* **3**, 342–356 (2023).
68. Dunham, E. M., Favreau, P. & Carlson, J. M. A supershear transition mechanism for cracks. *Science* **299**, 1557–1559 (2003).
69. Liu, Y. & Lapusta, N. Transition of mode II cracks from sub-Rayleigh to intersonic speeds in the presence of favorable heterogeneity. *J. Mech. Phys. Solids* **56**, 25–50 (2008).
70. Huang, Y. & Ampuero, J.-P. Pulse-like ruptures induced by low-velocity fault zones. *J. Geophys. Res.* **116**, 12307 (2011).
71. Ma, X. & Elbanna, A. E. Effect of off-fault low-velocity elastic inclusions on supershear rupture dynamics. *Geophys. J. Int.* **203**, 664–677 (2015).
72. Andrews, D. J. Rupture velocity of plane strain shear cracks. *J. Geophys. Res.* **81**, 5679–5687 (1976).
73. Das, S. & Aki, K. A numerical study of two-dimensional spontaneous rupture propagation. *Geophys. J. Int.* **50**, 643–668 (1977).
74. Ren, C. et al. Supershear triggering and cascading fault ruptures of the 2023 Kahramanmaraş, Türkiye, earthquake doublet. *Science* **383**, 305–311 (2024).
75. Liu, C. et al. Complex multi-fault rupture and triggering during the 2023 earthquake doublet in southeastern Türkiye. *Nat. Commun.* **14**, 5564 (2023).
76. Okuwaki, R., Yagi, Y., Taymaz, T. & Hicks, S. P. Multi-scale rupture growth with alternating directions in a complex fault network during the 2023 south-eastern Türkiye and Syria earthquake doublet. *Geophys. Res. Lett.* **50**, e2023GL103480 (2023).
77. Bizzarri, A., Dunham, E. M. & Spudich, P. Coherence of Mach fronts during heterogeneous supershear earthquake rupture propagation: simulations and comparison with observations. *J. Geophys. Res.* **115**, B08301 (2010).
78. Wu, F. et al. Pulse-like ground motion observed during the 6 February 2023 M_w7.8 Pazarcík earthquake (Kahramanmaraş, SE Türkiye). *Earthq. Sci.* **36**, 328–339 (2023).

Methods

Ground motion data

The velocity waveforms used in this study were obtained from the instrument-corrected strong ground motions. The unfiltered raw north–south, east–west and vertical acceleration records were obtained from AFAD and the Kandilli Observatory and Earthquake Research Institute, respectively (retrieved at 5:18 Pacific Standard Time on 9 February 2023)[2,23]. We computed the velocities for TK:NAR, TK:4615, TK:4611 and TK:4614 by numerically integrating the acceleration records from AFAD using the trapezoidal rule at the sampling frequency (100 Hz)[2]. We processed the velocity response for KO:KHMN using ObsPy software[79]. We then resolved the computed north–south and east–west ground velocity signals along the directions parallel and perpendicular to the Narli fault shown in Fig. 1. We note that there is some uncertainty in the estimate of the Narli fault strike and we explore the effect of variations in fault strike on the ratio of ground motion amplitudes in the Methods section 'Strike orientation uncertainty' and Extended Data Fig. 2.

A geometric interpretation of the ground velocity field structure

A simple justification for why the FP component of the ground velocity is more dominant than the FN component in the case of supershear propagation originates from the geometrical representation of the respective velocity fields of a singular shear crack propagating at these speeds. Both the supershear Mach front and the sub-Rayleigh rupture front are a superposition of S-wave fronts (as shown in Extended Data Fig. 1a) emitted by the propagating rupture. The displacement field lies tangent to the arc of the circular S wave. As shown in Extended Data Fig. 1b for a sub-Rayleigh rupture, the S-wave circular fronts pile up to form a locally concentrated field with a displacement field vector aligned perpendicularly to the propagating rupture, hence forming a dominant FN component. Since a supershear rupture propagates faster than the S-wave speed, instead of localizing, the rupture generates circular S-wave fronts that combine to form an inclined Mach front, as shown in Extended Data Fig. 1c. The resultant displacement field is oriented parallel to the shear Mach front. The normal to the Mach front forms an acute angle ϕ with the interface that remains the same for all S-wave fronts (the Mach cone itself propagates along that normal at S-wave speed). It then follows that as the rupture propagates faster than $\sqrt{2}C_s$ this acute angle becomes greater than $\pi/4$ and, accordingly, the shear Mach front becomes more aligned with the interface (angle θ, which forms between the Mach cone front and the interface, decreases to $<\pi/4$). Since the resultant displacement field is aligned with the Mach front, the displacement field becomes dominated by its FP component (we refer interested readers to Fig. 1 in ref. 44, Fig. 2 in ref. 26 and Fig. 1 in ref. 32).

Strike orientation uncertainty

In our analysis, we rely on the aftershock orientation to quantify the ratio of FP to FN ground velocity components. To address the uncertainty in this value, we consider multiple fault orientations. Extended Data Fig. 2 shows the ratio of FP to FN as the strike angle changes. Primarily, we observe that the ratio of FP to FN remains >1 at a strike angle of 16°. As the angle increases, the ratio between FP and FN also increases. Although there is uncertainty in the strike angle, we note that it is likely to be higher than 16° based on the aftershock sequence, fault trace mapping[22] and several other studies. For example, the USGS estimated the strike to be 28° (ref. 1), Delouis et al.[7] estimated it to be 30° and Okuwaki et al.[76] estimated it to be 35°. Accounting for uncertainty in the fault strike shows that the FP > FN pattern is preserved. This suggests that our assertion of supershear propagation is robust even in the presence of large uncertainties in the orientation of the Narli fault

Shock wave arrival at station TK:4614

To further explore our hypothesis of supershear propagation on the latter portion of the Narli fault, we analysed the ground motion records of station TK:4614, located at 37.48513° N, 37.29775° E. This station is located further away from the Narli fault at a vertical distance y_3 = ~9 km from the fault trace. This eliminates the possibility of conducting an FP-to-FN ratio analysis accurately. However, we can use phase arrival times to further corroborate our hypothesis. Extended Data Fig. 3a shows a schematic of a propagating supershear rupture on the Narli fault that transitioned at distance L_T from the hypocentre. As the rupture arrives at station TK:NAR (x_2, y_2), the rupture is already supershear and has a Mach front associated with it. We further assume that the rupture proceeds to propagate at constant speed V_r beyond TK:NAR (x_2, y_2) and towards EAF. The Mach front is thus straight and the speed of the normal to the Mach front is the S-wave speed, C_s. This implies that for a station located at $(\bar{x}, \bar{y})$, once the rupture tip arrives at point $\bar{x}$, the time taken for the Mach front to arrive at the station is given by $\bar{y}\cos(\theta)/C_s$ (as shown in Extended Data Fig. 3a), where, θ is the angle between the shear Mach front and the fault line and can be obtained through the relationship $\sin(\theta) = C_s/V_r$ (refs. 26,27). The time taken for the rupture tip to traverse from x_2 to x_3 is given by $(x_3 - x_2)/V_r$. The rupture speed V_r was already estimated to be ~$1.55C_s$ using the ratio of FP to FN components at the twin stations.

It follows that the time taken for the Mach front to arrive at station TK:4614 (x_3, y_3) from TK:NAR is given by $\Delta t_{4614} = (x_3 - x_2)/V_r + |y_3 - y_2|\cos(\theta)/C_s$ where $x_3 - x_2$ is the FP distance between the stations and y_2 and y_3 are the normal distances of each of the two stations from the fault line. There is some uncertainty in the values of y (due to fault orientation) and C_s. However, we estimate $|y_3 - y_2|$ to be ~7.2 km based on the assumed fault strike of 22° and assume C_s to be 3,320 m s^{-1}, as in the previous section. We then calculate the time taken for the shear Mach front to arrive at TK:4614 from TK:NAR to be Δt_{4614} = 4.4 s. Extended Data Fig. 3b shows the FP component of the velocity strong ground motion (the timing is unchanged by applying the common filtering between 0.01 and 10 Hz). We observe that ~4.13 s passed between the arrival of the strong signal (due to the shear Mach front) at TK:NAR and TK:4614, which is slightly shorter than the time difference we estimated above. Given the uncertainty in the fault orientation, the S-wave speed C_s and the possible acceleration of the rupture front beyond the instantaneous rupture speed estimated at the twin station, our estimated value for Δt_{4614} is in good agreement with the observed value.

Furthermore, in Extended Data Fig. 3c we show the FP and FN velocity ground motion records for station TK:4614. We observe a clear time shift between the dominant FP pulse (indicated by point B) and the trailing FN pulse (indicated by point C). As the rupture transitions to supershear at TK:4615, the remanence of the initial, sub-Rayleigh, rupture trails the supershear rupture front. This secondary pulse propagates at the Rayleigh speed (the red arc shown in Extended Data Fig. 3a) and is called the trailing Rayleigh pulse[26] associated with the transition. The ground motion pulse observed at point B, which has a larger FP component, is generated by the supershear Mach front, whereas pulse C, which carries almost entirely an FN component, arises from the trailing Rayleigh rupture.

The earlier arrival of an FP dominant pulse followed by the arrival of a dominant FN pulse is yet another clear indication of a transitioned supershear rupture that has been observed to occur in experiments, dynamic rupture models and kinematic source models[26,27,32,44,48]. Furthermore, this is similar to records from Denali's Pump Station 10 showing that the trailing Rayleigh pulse was only evident in the FN component[27,29,44]. To further corroborate this, we computed the difference between the arrivals of the shock front and the trailing Rayleigh as follows: $\Delta t = \frac{x_3 - x_2}{C_R} - \Delta t_{4614}$. Using the previously estimated parameters, this yields Δt_p = 0.3 s (the subscript p implies the predicted quantity). The same quantity may also be measured directly from the two ground motion records as the time difference between points B and C in Extended Data Fig. 3c. This difference is 0.24 s, which is in good agreement with the theoretical estimate based on the assumption of a transition to supershear.

Next, and for the sake of completeness, we consider the alternative hypothesis under which the rupture only propagated at a sub-Rayleigh speed and never transitioned to supershear throughout the Narli fault. We see that this scenario contradicts the available observations. First, we note that the stations TK:NAR and TK:4614 are radially separated by 16 km based on the relocated epicentral location (37.2444° N, 37.0234° E)[3]. This radial distance is relatively insensitive to uncertainties in epicentral location as it remains 16 km using alternative epicentral location estimates, such as those reported by the USGS or AFAD[1,2]. We then compute the average speed of wave propagation between the two stations (using the radial distances and the difference in arrival times) to be ~3.9 km s^{-1}, which far exceeds the S-wave speed C_s for the region[50,51]. This further supports our initial hypothesis that the rupture transitioned to supershear.

Station TK:4611

To support our conclusion of supershear rupture on the Narli fault, we use additional strong ground motion records from station TK:4611. As shown in Extended Data Fig. 4, station TK:4611 lies along the virtual extension of the Narli fault, past its junction with the EAS, and is located at a distance of 42 km from TK:NAR (the twin station). In Extended Data Fig. 4a, we evaluate the arrival time of the initial disturbance associated with the S waves travelling to station TK:4611 (point B) in reference to the corresponding arrival time at TK:NAR (point A). We observe that the arrival at TK:4611 occurs at ~10 s. This is then followed by multiple arrivals with a maximum peak at ~20 s. Since the two stations are aligned with the Narli fault, this produces an average wave propagation speed of ~4.2 km s^{-1}. This value far exceeds the estimated S-wave speed of the region[50,51]. At first glance, this indicates that at least for a portion of the propagation the waves travelled at supershear speeds.

There could be multiple explanations for this observed fast arrival time. First, a supershear rupture propagation on the Narli fault would send arrest signals as it encounters the junction with the EAF and thus contributes to a faster-than-usual wave arrival speed. Based on dynamic rupture modelling, once a supershear rupture is arrested it generates three distinct signals[36]. A wave field is generated at the arrested rupture tip, which attenuates with distance but propagates at a speed lower than the rupture speed but faster than the S-wave speed. This wavelet is followed by shear and Rayleigh Mach waves propagating at the S-wave speed. Based on the fast arrival of such arrest waves (propagating at a speed larger than the S-wave speed) at TK:4611, we expect this signal to be associated with the initial wave field generated at the tip. Second, this early arrival could be a detached shear Mach front from an early transition on the northeast branch of the EAF to supershear speeds. This is indeed possible; however, we highlight that from a physical standpoint this conclusion would also support supershear rupture propagation on the Narli fault. Indeed, numerous experimental and numerical studies[60–62] have shown that when a rupture encounters a branch or a junction, its propagation speed decreases. Accordingly, if the rupture propagated as supershear on the northeast segment, it is expected to have been supershear on the Narli fault before encountering the junction. Third, it is possible that material heterogeneity between the two stations manifested in regions of higher C_s, causing waves to propagate faster. However, this would be highly unlikely to have such a pronounced effect due to the closeness of the two stations and the fact that an S-wave speed of 4.2 km s^{-1} is fairly high for the regional average[50,51]. Although the specifics of supershear rupture arrest warrant further study, the unusually fast arrival time between TK:4611 and TK:NAR provides further supporting evidence that a portion of the rupture propagating along the Narli fault was indeed supershear.

We further explored the nature of the ground motion characteristics in the record of TK:4611. Since the signal is not directly associated with any rupture propagation on the Narli fault (the Narli fault line does not continue beyond its junction with EAF), we cannot strictly rely on the theoretical FP-to-FN ratio argument. However, we still note that the FP component of the signal remains larger than the FN component. This could be due to the arrival of the arrest phase at the station, which still carries a larger FP component. Similar observations were made numerically by Vyas et al.[36] regarding radiated waves from arrested supershear ruptures. Furthermore, in the first signal received by the station, we observe a difference in arrival time between the peak FP component (point C) and the peak FN component (point D). The earlier arrival of the FP peak is consistent with supershear characteristics, as noted earlier and extensively discussed by Aagaard and Heaton[48] and Hu et al.[34]. This also provides further supporting evidence for supershear propagation along the Narli fault.

Data availability

The mapped surface rupture data are from ref. 22. All of the ground motion records used in this study were obtained from AFAD[2] and the Kandilli Observatory and Earthquake Research Institute[23] and processed using ObsPy[79]. Figure 1 was produced using QGIS based on map data from Natural Earth.

References

79. Beyreuther, M. et al. ObsPy: a Python toolbox for seismology. *Seismol. Res. Lett.* **81**, 530–533 (2010).

Acknowledgements

The ground motion data used in this study can be obtained from AFAD, USGS and the Kandilli Observatory and Earthquake Research Institute. We thank AFAD for setting up dense near-fault observatories and immediately publishing openly accessible data from a huge number of accelerometers during these trying times for Turkey. A.R. acknowledges support from the Caltech/Mechanical and Civil Engineering Big Ideas Fund and Caltech Terrestrial Hazard Observation and Reporting Center. He also acknowledges support from the National Science Foundation (grants EAR-1651235 and EAR-1651235). A.E. acknowledges support from the Southern California Earthquake Center, through a collaborative agreement between the National Science Foundation (grant EAR0529922) and USGS (grant 07HQAG0008), and National Science Foundation CAREER award 1753249 for modelling complex fault zone structures.

Author contributions

A.R. conceived of and supervised the study. All authors contributed to analysis of the ground motion data, drafted the paper and participated in its revision and finalization.

Competing interests

The authors declare no competing interests.

Additional information

Extended data is available for this paper at https://doi.org/10.1038/s41561-025-01707-2.

Correspondence and requests for materials should be addressed to Ares Rosakis, Mohamed Abdelmeguid or Ahmed Elbanna.

Peer review information *Nature Geoscience* thanks Alice Gabriel and the other, anonymous, reviewer(s) for their contribution to the peer review of this work. Primary Handling Editor: Tamara Goldin, in collaboration with the *Nature Geoscience* team.

https://doi.org/10.1038/s41561-025-01707-2

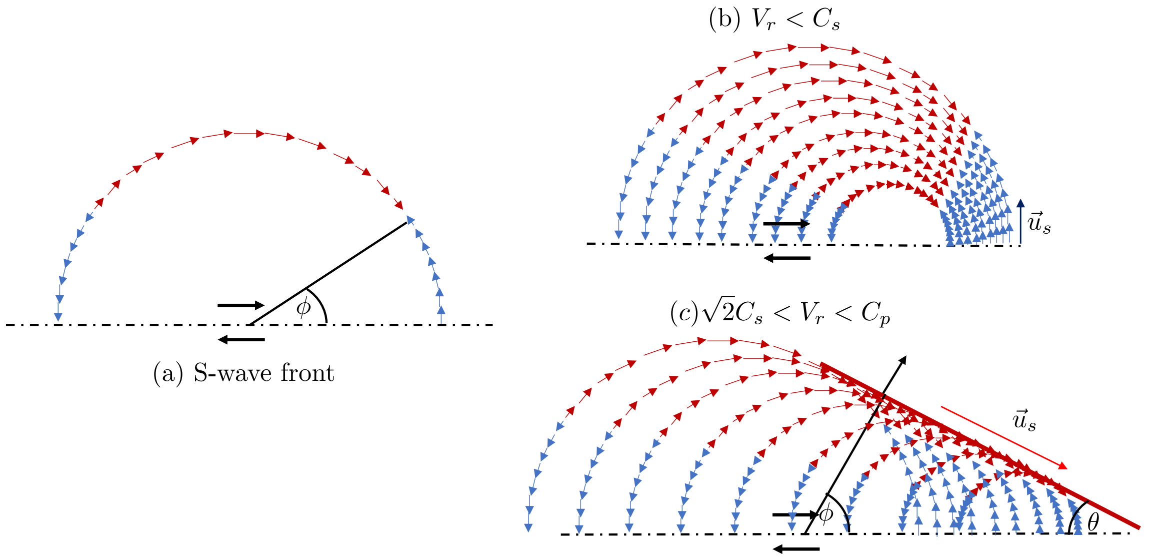

(a) S-wave front

(b) $V_r < C_s$

(c) $\sqrt{2}C_s < V_r < C_p$

Extended Data Fig. 1 | Geometric characteristics of sub-shear and supershear (super-Eshelby) propagation. (**a**) Shear wavelets emitted by a shear dislocation form. Superposition of shear wavelets leads to the formation of (**b**) sub-Rayleigh rupture and (**c**) shear Mach front of a supershear rupture. Figure reproduced with permission from ref. 32, Elsevier.

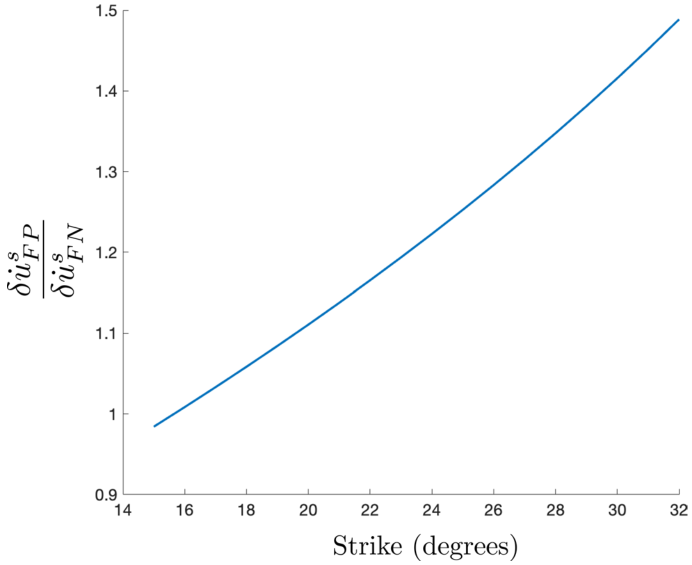

Extended Data Fig. 2 | The dependency of the ratio of the FP to FN component on the strike angle of the Narli fault. The ratio of the FP to FN component is greater than 1 at a strike angle of 16° and increases further as the angle increases.

https://doi.org/10.1038/s41561-025-01707-2

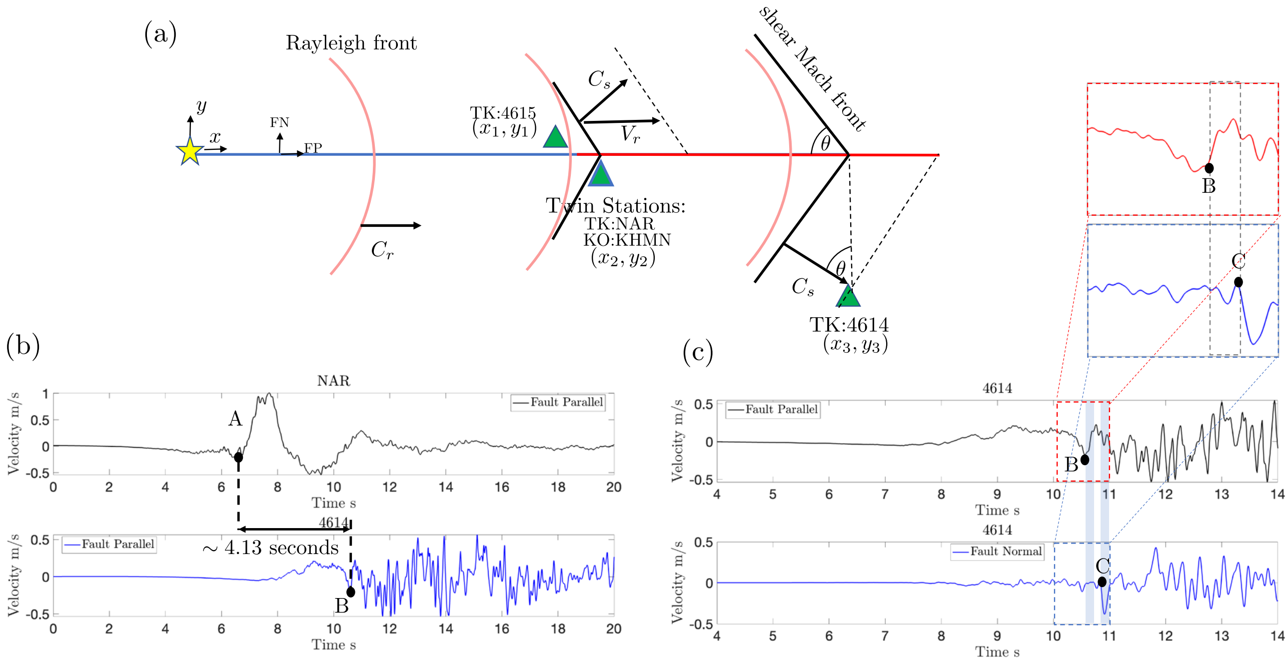

Extended Data Fig. 3 | The arrival of shock front at TK:4614. (**a**) A to-scale schematic of the location of the TK:4614 station relative to station TK:NAR and the epicenter. Green triangles indicate the location of the stations. The epicenter is marked by a yellow star. The red front indicates the shear wave propagation front while the straight black lines represent the shock fronts (Mach lines) associated with supershear speeds. Station TK:4614 is located further away from the Narli fault relative to TK:NAR or TK:4615 rendering theoretical estimates of local rupture speed using ground motion record complex. (**b**) The strong ground motion at stationS TK:NAR and TK:4614 shows the phase arrival times between the two stations. (**c**) The strong ground motion (FN and FP) at TK:4614 shows a clear separation between the arrival of the initial peak of the FP and FN components.

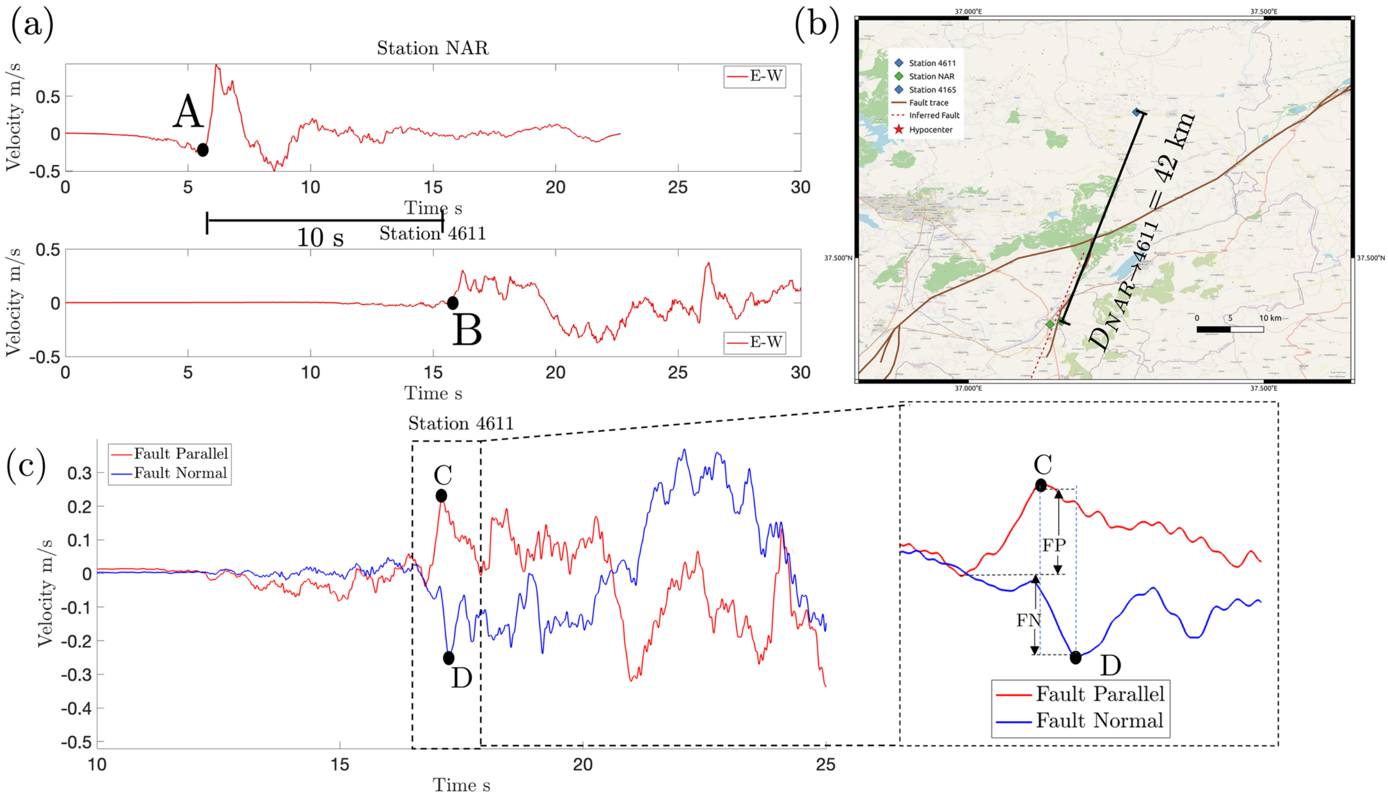

Extended Data Fig. 4 | Supporting evidence of supershear transition on the Narli fault. (**a**) The strong ground motion records showing the E-W component of velocity at both stations TK:NAR (one of the twin stations) and TK:4611. Points A and B highlight the first arrival of shear waves to the respective stations. (**b**) A map highlighting the location and distance of the two stations with respect to one another. (**c**) The strong ground motion records showing the FP and FN components of velocity at station TK:4611. Basemap data from OpenStreetMap contributors, 2024.